

Cloud structure and young star distribution in the Dragonfish complex

Nestor Sanchez¹, Elisa Nespoli¹, Marta Gonzalez¹, and Juan B. Climent^{1,2}

¹Universidad Internacional de Valencia (VIU), C/Pintor Sorolla 21, E-46002 Valencia, Spain

²Departament d'Astronomia i Astrofísica, Universitat de València, Burjassot, E-46100, Spain

Received ...; accepted ...

ABSTRACT

Context. Star formation is a complex process involving several physical mechanisms interacting with each other at different spatial scales. One way to shed some light on this process is to analyse the relationship between the spatial distributions of gas and newly-formed stars. In order to obtain robust results, it is necessary for this comparison to be made using quantitative and consistent descriptors applied to the same star-forming region.

Aims. Here, we use fractal analysis to characterise and compare in a self-consistent way the structure of the cloud and the distribution of young stellar objects (YSO) in the Dragonfish star-forming complex.

Methods. Different emission maps of the Dragonfish Nebula were retrieved from the NASA/IPAC Infrared Science and the Planck Legacy archives. Moreover, we used photometric information from the AllWISE catalogue to select a total of 1082 YSOs in the region, for some of which we derived physical properties from their spectral energy distributions (SEDs). For both datasets (cloud images and YSOs), the three-dimensional fractal dimension (D_f) was calculated using previously developed and calibrated algorithms.

Results. The fractal dimension of the Dragonfish Nebula ($D_f = 2.6 - 2.7$) agrees very well with values previously obtained for the Orion, Ophiuchus, and Perseus clouds. On the other hand, YSOs exhibit on average a significantly smaller value ($D_f = 1.9 - 2.0$) that indicates a much more clumpy structure than the material from which they formed. Younger Class I and Class II sources have smaller values ($D_f = 1.7 \pm 0.1$) than more evolved Transition Disk objects ($D_f = 2.2 \pm 0.1$), evidencing a certain evolutionary effect where an initially clumpy structure tends to gradually disappear over time.

Conclusions. The Dragonfish complex exhibits a structure similar to that of other molecular clouds in the Galaxy. However, we have found clear and direct evidence that the clustering degree of the newly born stars is significantly higher than that of the parent cloud from which they formed. The physical mechanism behind this behaviour is still not clear.

Key words. ISM: clouds – ISM: structure – ISM: individual objects: Dragonfish Nebula – Stars: early-type – Stars: formation

1. Introduction

Star formation is a complex process that is still not fully understood. There is an accepted general picture in which gas and dust inside giant molecular clouds (GMCs) gravitationally collapse to form groups of protostars. After this, protostellar winds and jets blow away the surrounding clouds leaving behind clusters of newly formed stars (see, for instance, the review by McKee & Ostriker 2007). However, the details of the process are much more complex than this. The internal structure of GMCs is mainly driven by turbulent motions whose origin is still under debate (Larson 1981; Elmegreen & Scalo 2004; Smith et al. 2022). Turbulence tends to act against the gravitational collapse, but it can also originate shocks and high-density regions promoting the collapse. Apart from turbulence and self-gravitation, there are other physical mechanisms such as magnetic fields, thermal pressure and radiation fields that may play important roles at different spatial scales and in different moments of the star formation process (McKee & Ostriker 2007). Stellar feedback from newly formed stars injects energy into the medium that can either disperse the gas (preventing the formation of other stars) or compress it (triggering the formation of additional stars) depending on many different factors (Bally 2016). Even if very few physical mechanisms were considered, the interaction among all the involved processes and the interaction among different regions of the GMC at different spatial scales convert star

formation in a highly non-linear chaotic process, in the sense of being very sensitive to small variations on the initial and environmental conditions (Sánchez & Parravano 1999; Jaffa et al. 2022).

The study of the star formation process may be divided into two steps. Firstly, one needs to address the initial distribution of gas and dust in GMCs, i.e. the initial conditions of the process. Secondly, one can focus on the way and degree in which this initial distribution is transferred or converted into new-born stars, i.e. the star formation process itself. Each one of these parts is a complex research line with many physical processes and many observational problems involved. A way to yield some light into the problem is using a two-sided approach. On the one hand, to study and characterise in detail the structure and properties of GMCs that represent the initial conditions of the star formation process. On the other hand, to analyse the distribution and properties of YSOs. The comparison of these two parts may help to understand the process from which the parental cloud is transformed into newly-formed stars. In order to draw solid conclusions, this comparison should be made for the same star-forming region and using quantitative and consistent descriptors. In the literature, several descriptors and techniques have been considered for the characterisation of the internal structure of interstellar clouds, such as structure tree methods (Houllahan & Scalo 1992), Delta-variance techniques (Stutzki et al. 1998; Elia et al.

2014; Dib et al. 2020), principal component analysis (Ghazali et al. 1999), metric space techniques (Khalil et al. 2004; Robitaille et al. 2010), dendrograms (Rosolowsky et al. 2008; Colombo et al. 2015), convolutional neural networks (Bates et al. 2020; Bates & Whitworth 2023), and fractal (Falgarone et al. 1991; Vogelaar & Wakker 1994; Sánchez et al. 2005, 2007b; Lee et al. 2016; Marchuk et al. 2021) and multifractal (Chappell & Scalo 2001; Khalil et al. 2006; Elia et al. 2018) analysis, among others. Regarding the structure of the distribution of formed stars and star clusters, commonly used methods include simple kernel density estimators (Silverman 1986), the nearest neighbour distribution and the two-point correlation function (see, for instance, Gomez et al. 1993; Larson 1995; Simon 1997; Hartmann 2002; Kraus & Hillenbrand 2008). The correlation function may be used to directly estimate the fractal correlation dimension of star and cluster distributions (de La Fuente Marcos & de La Fuente Marcos 2006; Kraus & Hillenbrand 2008; Sánchez et al. 2007a; Sánchez & Alfaro 2009). A different method was introduced by Cartwright & Whitworth (2004) which proposed the use of the so-called Q -parameter, calculated from the minimum spanning tree, to quantify the spatial substructure. This method has the advantage of being able to distinguish between centrally concentrated and fractal-like distributions, and it has been widely used in different star-forming regions (see, for example, Jaffa et al. 2017; Hetem & Gregorio-Hetem 2019, and references therein). Other more recent techniques or variants of already established methods to characterise the internal structure of interstellar clouds and young stars or star clusters include the INDICATE tool (Buckner et al. 2019; Blaylock-Squibbs et al. 2022), the S2D2 procedure (González et al. 2021), the Moran's I statistic (Arnold et al. 2022), and the RJ Plots (Jaffa et al. 2018; Clarke et al. 2022).

Each method has its advantages, disadvantages, and limitations, and the choice of which to use depends, among other factors, on the scientific goal to be addressed. Fractal analysis is a particularly suitable tool because of the observed hierarchical and self-similar structure of the interstellar medium, which resembles a fractal system (see Bergin & Tafalla 2007, and references therein). In fractal analysis, the degree of spatial heterogeneity can be quantified through a simple parameter: the fractal dimension (D_f). One advantage of this approach is that D_f can be calculated for both continuous and discrete structures, which allows a direct comparison between the distribution of gas and dust in the parental cloud and the distribution of newly-formed stars. It is believed that very young stars and clusters should follow the fractal patterns of the interstellar medium from which they formed but that such patterns could be dissipated on short timescales (Goodwin & Whitworth 2004; Sánchez & Alfaro 2009; Allison et al. 2010; Sun et al. 2022). However, it is not clear whether the wide variety of observed spatial patterns is due to differences in the structure of the original clouds or to evolutionary or environmental effects (Goodwin & Whitworth 2004; Allison et al. 2010; Ballone et al. 2020; Daffern-Powell & Parker 2020; González et al. 2021).

In this work, we use fractal analysis to examine in a systematic and consistent way the distribution of gas and YSOs in the Dragonfish region. Dragonfish (G298.4-0.4) is a star-forming complex located at $(l, b) = (298, 0.4)$ deg first detected by Russell (1997) as a clump of HII regions at 10 kpc. Some authors suggested that the Dragonfish complex contained a supermassive OB association (Rahman et al. 2011a,b). However, a detailed work by de la Fuente et al. (2016) showed that such an association does not exist and that the existing young massive clusters and Wolf-Rayet stars can explain most of the observed

ionisation. de la Fuente et al. (2016) estimated that this region is located at the outer edge of the Sagittarius-Carina spiral arm, at a distance of $d = 12.4$ kpc. However, Rate et al. (2020) found a much closer distance of 5.2 kpc using data from the Gaia DR2, although they warned that their distance estimation may be inaccurate. Previous studies suggest that Dragonfish is among the largest and most massive cloud complexes in the Milky Way (see de la Fuente et al. 2016, and references therein), which makes it an interesting region to investigate the star formation process. Section 2 of this work is dedicated to characterise the distribution of gas and dust in the Dragonfish nebula. In Section 3 we use photometric information in several bands to search for YSOs, determine their physical properties, and study the spatial and hierarchical clustering of the selected YSOs. A comparison between the distributions of gas and YSOs is given in Section 4 and, finally, Section 5 summarises our main conclusions.

2. Gas and dust distribution

2.1. Used data

We selected a region large enough to cover the entire Dragonfish star-forming complex. The region is defined by the galactic coordinates $l = (297.0, 299.5)$ deg and $b = (-1.1, +0.8)$ deg. By using the NASA/IPAC Infrared Science Archive¹, we downloaded images from the Infrared Array Camera (IRAC) of the Spitzer mission (Werner et al. 2004) and created a mosaic of the region using the Montage program². We performed this process for the four IRAC channels. The obtained results did not show significant differences among the four channels, so we present here the results using the $8 \mu\text{m}$ IRAC channel only, namely channel 4. We also searched for additional data in other wavelengths but radio maps usually do not have enough spatial resolution to achieve our science goals. A relatively good enough image at microwave wavelengths was obtained from the Planck mission (Planck Collaboration et al. 2011). In particular, we downloaded from the Planck Legacy Archive³ the map of the HFI 545 GHz channel ($550 \mu\text{m}$). Figure 1 displays the maps from Spitzer and Planck used in this study. In general, these maps trace the distribution of gas and dust in the Dragonfish Nebula. The Planck map is basically a thermal dust emission map (Planck Collaboration et al. 2016) whereas IRAC channel 4 is dominated by polycyclic aromatic hydrocarbon (PAH) emission (Draine & Li 2007), which tends to spatially correlate with molecular gas (Schinnerer et al. 2013).

2.2. Fractal dimension

In this section, we use fractal analysis to study the distribution of gas and dust in the Dragonfish region. This tool uses only one parameter, the fractal dimension D_f , to characterise the manner in which the gas is distributed. A D_f value of 3 indicates a homogeneous three-dimensional spatial distribution, while progressively smaller values of D_f correspond to increasingly irregular distributions with higher degrees of clumpiness (Mandelbrot 1983). Monofractal clouds can be characterised by a single D_f value that is valid across the entire range of spatial scales over which the gas is distributed. Although some evidence of multifractality in the interstellar medium (ISM) has been reported (Chappell & Scalo 2001), this remains an open issue, and a systematic anal-

¹ <https://irsa.ipac.caltech.edu>

² <http://montage.ipac.caltech.edu/>

³ <https://pla.esac.esa.int>

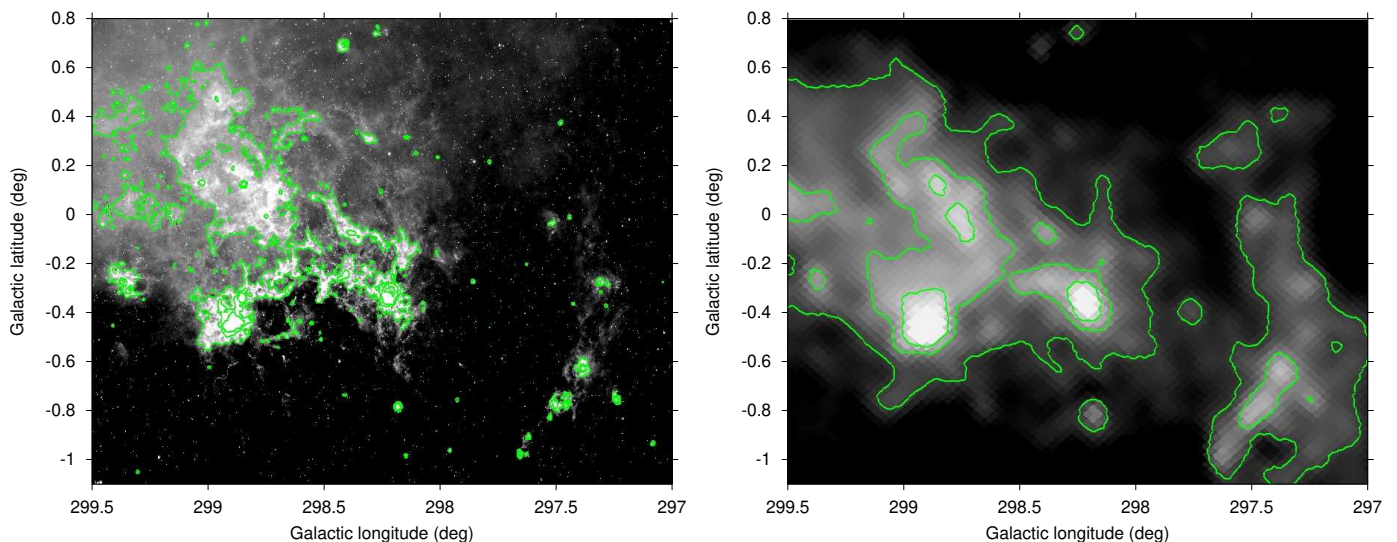


Fig. 1. Images of the Dragonfish Nebula covering the region studied in this work. *Left panel:* Mosaic obtained by assembling 27 Spitzer IRAC images in the $8\ \mu\text{m}$ band. *Right panel:* map retrieved from the Planck Legacy Archive (HFI 545 GHz data). Both maps are in logarithmic grey scale and, for reference, three contours have been drawn at 30, 60 and 100 MJy/sr (Spitzer map) and at 100, 150 and 200 MJy/sr (Planck map).

ysis assuming a nearly monofractal behaviour may still provide valuable insights into the underlying structure of the ISM.

In general, interstellar clouds are observed as two-dimensional images projected onto the celestial sphere. Therefore, to study the fractal properties of clouds, many authors use the so-called perimeter-area relation to calculate the dimension of the contours of the projected clouds (Bazell & Desert 1988; Dickman et al. 1990; Falgarone et al. 1991; Hetem & Lepine 1993; Vogelaar & Wakker 1994; Sánchez et al. 2005; Marchuk et al. 2021), that we denote as D_{per} . In general, the relation between 2D and 3D fractal dimension values is not trivial but in principle D_{per} can only vary between the theoretical limits of $D_{per} = 1$ for the case of smooth projected contours and $D_{per} = 2$ for extremely irregular contours (see discussions in Beattie et al. 2019; Sánchez et al. 2005). In previous works (Sánchez et al. 2005, 2007b), we implemented and optimised an algorithm to estimate D_{per} in a reliable way in cloud emission maps. The method defines objects as sets of connected pixels with intensity values above a defined threshold. In order to increase the number of objects, the algorithm uses ~ 20 brightness levels equally spaced between the minimum and the maximum brightness of the map. Several tests performed with both simulations and real maps showed that the obtained D_{per} values do not depend on the exact number of brightness levels as long as they are not too few (≤ 5). Then, the perimeter and area of each object in the image are calculated and the best linear fit is determined in a $\log(\text{perimeter})$ - $\log(\text{area})$ plot, being $D_{per}/2$ the slope of the fit (Mandelbrot 1983). The algorithm was optimised to account for problems occurring at the image edges as well as signal-to-noise ratio and resolution effects. More importantly, this algorithm was used to characterise in detail the relationship between D_{per} and D_f . The relation $D_{per} - D_f$ was empirically determined by simulating three-dimensional clouds with well-defined fractal dimensions and projecting them onto random planes. In general and as expected, D_{per} decreases (more convoluted boundaries) as D_f increases (more irregular and fragmented clouds). However, the exact relation is not a simple function and, as the image resolution decreases, there is a tendency of D_{per} to decrease because the details of the roughness disappear as the pixel size increases. The calculated functional forms relating D_{per} , D_f and N_{pix} (the

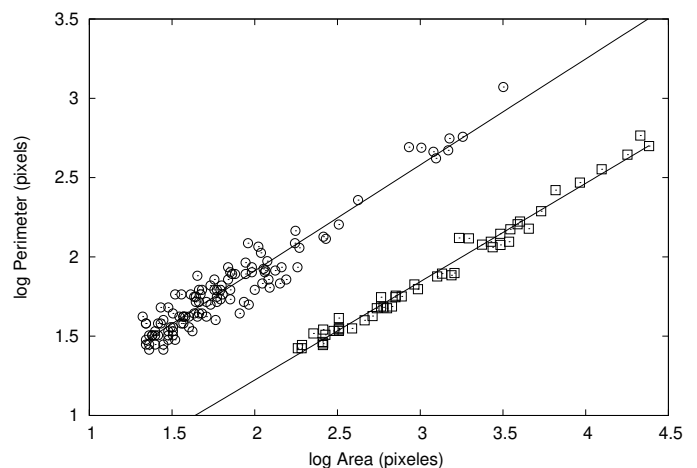


Fig. 2. Perimeter as a function of the area in pixels for objects (clouds) in the Dragonfish Nebula using the Spitzer (open circles) and the Planck (open square) maps. Planck data have been vertically shifted by -0.5 for clarity. Solid lines are the corresponding best linear fits for all the data points.

Table 1. Perimeter-area based dimension (D_{per}) and three-dimensional fractal dimension (D_f) for the Spitzer and Planck maps shown in Fig. 1.

Map	Pixels	D_{per}	D_f
Spitzer	1525×939	1.34 ± 0.04	$2.6 - 2.7$
Planck	697×549	1.24 ± 0.02	$2.6 - 2.7$

maximum object size in pixel units) were presented in Fig. 8 and Table 1 of Sánchez et al. (2005) and are used here to estimate D_f for the Dragonfish Nebula.

We applied the previously described algorithm to the maps shown in Fig. 1. The obtained perimeter-area relations are shown in Fig. 2. The corresponding fractal dimension values are summarised in Table 1, where D_f is estimated from D_{per} based on the simulations of projected clouds performed in Sánchez et al. (2005). The Spitzer map we are using has a pixel size corre-

sponding to the “good resolution” case in Sánchez et al. (2005, see Fig. 8 and Table 1 in this paper), i.e. the case with $N_{pix} \geq 400$ where N_{pix} is the maximum object size in pixel units. In contrast, the Planck map has a pixel size corresponding to the case $N_{pix} \approx 200$. Thus, the relatively small D_{per} value of the Planck map in Table 1 is due to resolution effects that tend to smooth the contours. For this reason, after correcting for resolution effects, the three-dimensional fractal dimensions result in the same value for both maps. The obtained value $D_f = 2.6-2.7$ for the Dragonfish Nebula agrees with our previous results for emission maps in different molecular lines of the Orion, Ophiuchus, and Perseus clouds, where the fractal dimensions are always in the range $2.6 \leq D_f \leq 2.8$ (Sánchez et al. 2005, 2007b). These D_f values are significantly higher than the average value $D_f \approx 2.3$ commonly assumed for the ISM (Elmegreen & Elmegreen 2001).

3. Young stellar object candidates

3.1. Candidate selection

Within the selected region, we used VizieR⁴ (Ochsenbein et al. 2000) to search for all existing sources in the AllWISE catalogue (Wright et al. 2010; Cutri et al. 2021). A total of 110 401 sources were retrieved including their IDs, positions and photometry in the $W1 - W4$ and JHK bands. Then, we applied the multicolour criteria scheme proposed by Koenig & Leisawitz (2014) to identify YSO candidates. This selection scheme is based on applying different cuts in colours and magnitudes in the WISE+2MASS bands to remove contaminants (Star-forming galaxies, Active Galactic Nuclei, and Asymptotic Giant Branch stars) and to select YSOs of Classes I, II, and Transition disks. The application of these criteria to our sample yielded a total of 1082 YSOs, of which 139 belong to Class I, 627 to Class II, and 316 are Transition disk sources. Table 2 (fully available online) presents a list of the selected YSOs, including their properties as derived in this work. An example colour-colour diagram is shown in Fig. 3.

Of the selected sample, 323 sources had already been reported either as YSOs or YSO candidates by other authors (Lumsden et al. 2013; Marton et al. 2016; Kuhn et al. 2021; Rimoldini et al. 2023; Zhang et al. 2023). Table 2 also includes the references for these previously identified YSOs. The remaining YSOs are new candidates, identified for the first time in this work.

3.2. Physical properties of the selected YSOs

3.2.1. Distances

From the 1082 selected YSOs, there are 135 objects that have counterparts in the Gaia DR3 catalogue and therefore have available parallaxes. For these sources, we estimated their distances D from their parallaxes, taking into account the global parallax offset of -0.017 mas reported by Lindegren et al. (2021). In general, the obtained values of D are distributed over a relatively large range of values, due in part to uncertainties in the parallaxes (see Fig. 4). The most frequent value is found around $D \approx 4000$ pc. If we consider parallaxes with relatively smaller errors (purple histogram in Fig. 4), the distribution changes slightly but the mode of the distribution always remains in the range 3000 – 5000 pc. A distance of $D \sim 4 \pm 1$ kpc to the Dragonfish Complex is smaller than some previous estimations of $\sim 10 - 12$ kpc (de la Fuente et al. 2016; De Buizer et al. 2022) but consistent with the $\sim 4 - 5$ kpc reported by other authors (Moisés et al. 2011; Rate et al. 2020).

⁴ <https://vizier.cds.unistra.fr/>

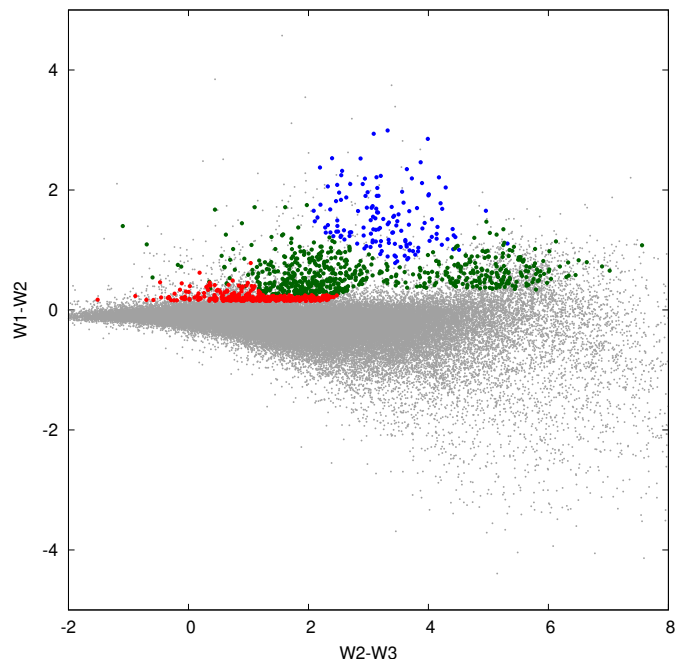


Fig. 3. Colour-colour diagram, $W1 - W2$ versus $W2 - W3$, for all stars in the sample (grey dots) and for sources fulfilling criteria of Class I (blue dots), Class II (green dots) and Transition disk (red dots) objects.

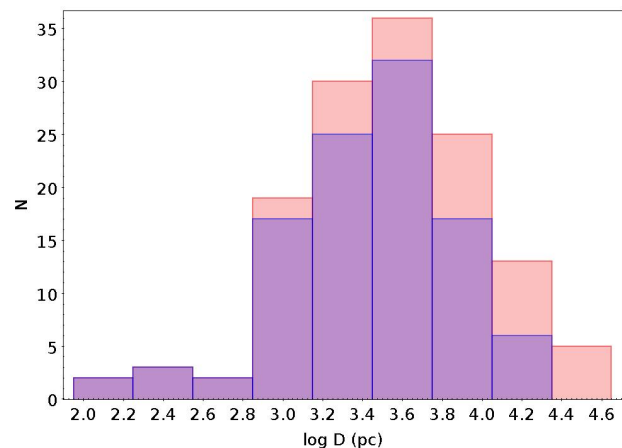


Fig. 4. Distribution of distances obtained from the parallaxes for the 135 stars that have counterparts in Gaia DR3. The purple histogram refers to sources having parallax errors smaller than the parallax values themselves.

3.2.2. Spectral energy distributions

The SEDs of the 1082 selected YSOs were analysed using the Virtual Observatory SED Analyzer (VOSA) developed by the Spanish Virtual Observatory (see details on the operation and limitations of VOSA in Bayo et al. 2008). VOSA is a tool that provides a friendly and flexible environment for finding the theoretical spectral model that best fits the observed photometric data. VOSA allows users to search and expand available photometry, choose from a list of models, and define parameter ranges to search for the best fit. For the fitting procedure, we first requested VOSA to expand the SEDs with all the photometry it could find. VOSA itself handles outlier rejection and, in case of finding different photometric values for the same filters, it calculates and uses an average value for the final SED.

Table 2. List of identified YSOs in the Dragonfish region. Here we show only a portion of the table for guidance regarding its form and content. The full version is available online and includes IDs from AllWISE, galactic and equatorial coordinates (J2000) in decimal degrees, magnitudes and errors in the WISE bands, object class according to Koenig & Leisawitz (2014)’s criteria, best model used for SED fitting, derived effective temperatures (K) and visual extinctions (mag), references for previously identified sources, and parallaxes and errors for the 135 stars having counterparts in the Gaia DR3 catalogue.

ID(AllWISE)	RA	DEC	W1	W2	W3	W4	Class	Model	T_{eff}	A_V
J115840.15-631550.4	179.667315	-63.264010	12.433	12.225	9.906	7.442	TrDisk			
J115905.16-631608.3	179.771510	-63.268990	11.481	11.227	9.321	7.164	Class II			
J115908.32-631559.7	179.784677	-63.266603	11.239	10.919	9.663	7.551	Class II			
J115915.50-631310.4	179.814600	-63.219573	9.368	8.352	7.607	4.957	Class II	BT-Settl	2600.0	2.0
J115917.83-630950.1	179.824294	-63.163930	11.749	11.571	10.719	8.405	TrDisk			

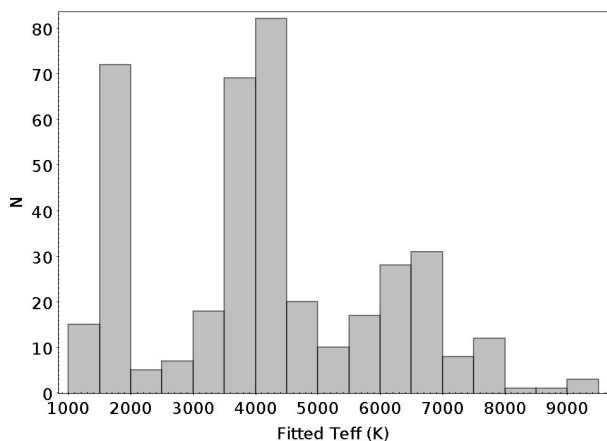


Fig. 5. Distribution of effective temperatures for the 399 sources whose SEDs could be fitted using VOSA (details in text).

We then requested VOSA to fit the SEDs by minimising the reduced chi-square with the latest version of the BT-Settl models, which are based on the CIFIST photospheric solar abundances (Caffau et al. 2011). The effective temperature (T_{eff}) is left as a free parameter in the fitting process, which in the BT-Settl models ranges from $1200 \leq T_{eff} \leq 7000$ K. VOSA fits the points of the SED that have not been flagged with possible infrared excess, which it assumes to be around the W1 band. The fitting process in VOSA is not very sensitive to some parameters such as metallicity and $\log g$ (Bayo et al. 2008). We made several tests by fixing or constraining these parameters around the expected values and also leaving them completely free, and in general the resulting fits were not significantly affected. Eventually, we left $\log g$ as a totally free parameter and fixed the metallicity to the solar value, whereas the visual extinction (A_V) was allowed to vary in the range $0 \leq A_V \leq 10$ mag. For those sources for which the fitting process did not converge on reasonable solutions we also tried an independent fitting with the ATLAS9 Kurucz ODFNEW/NOVER models (Castelli et al. 1997). For these cases the temperature can vary in the range $3500 \leq T_{eff} \leq 50000$ K and the rest of the parameters are set to the same conditions employed for the BT-Settl fits. In any case, all 1082 SEDs and their fits were visually examined to verify the adequacy of the fits and solutions found by VOSA.

For a total of 399 sources (37%), the corresponding SED was well fitted with either BT-Settl models (89% of the sources) or Kurucz models (11%). The temperatures T_{eff} and extinctions A_V that provided the best fits are reported in Table 2, and a histogram with the distribution of T_{eff} values is shown in Fig. 5. Around $\sim 50\%$ of the sources have photospheric temperatures in the range $3000 \lesssim T_{eff} \lesssim 5000$ K, although there is also a significant population of cool stars (late Ms or brown dwarfs) with

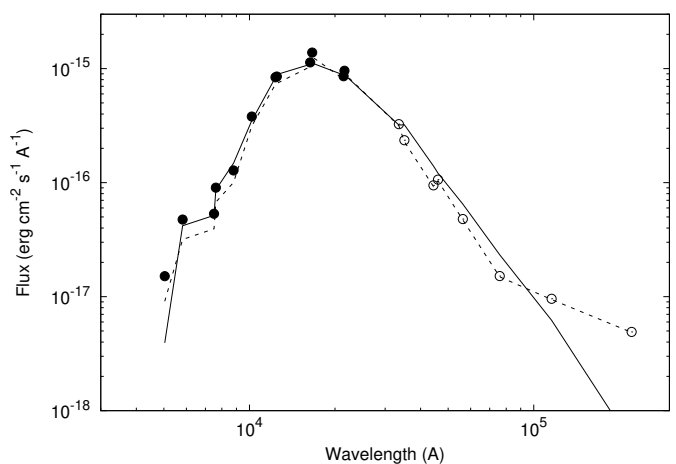


Fig. 6. Observed and best-fitted flux densities for one example source, J120022.63-631523.2, for which we obtained $T_{eff} = 1700$ K and $A_V = 0.5$, which is a Transition Disk object according to Koenig & Leisawitz (2014)’s criteria. Dashed line indicates the observed photometric data. Circles represent dereddened data, where solid circles denote data points that have been considered in the fitting process by VOSA. Solid lines indicate the best-fitted BT-Settl model. Some infrared excess is evident at wavelengths larger than $\sim 10 \mu\text{m}$.

$T_{eff} \lesssim 2000$ K). An example SED for the first star belonging to this group in our Table 2 is shown in Fig. 6, where we can see both the fit performed by VOSA using a BT-Settl model as well as the expected infrared excess likely produced by circumstellar dust. We have not detected significant patterns or correlations of T_{eff} or A_V with the spatial distribution or with any other relevant physical variable. This population of cool stars is subject to ongoing investigation.

3.3. Spatial distribution

The spatial distribution of the selected YSOs, overlaid on the Spitzer map at $8 \mu\text{m}$, is shown in Fig. 7. At first glance, younger classes (I and II) seem to follow the distribution of gas and dust exhibiting some level of clumpiness, whereas Transition disk sources tend to be more homogeneously spread through the region. In order to objectively quantify the clumpiness we use the so-called correlation dimension (D_c), which is suitable for analysing distributions of point sources. The correlation dimension measures the variation (as r increases) of the probability that two randomly chosen points are separated by a distance smaller than r (Grassberger & Procaccia 1983). For homogeneous point distributions in space it is expected that $D_c = 3$, whereas in a plane $D_c = 2$. If the points are distributed following fractal patterns then $D_c < 3$ in the space or $D_c < 2$ in the plane. Here,

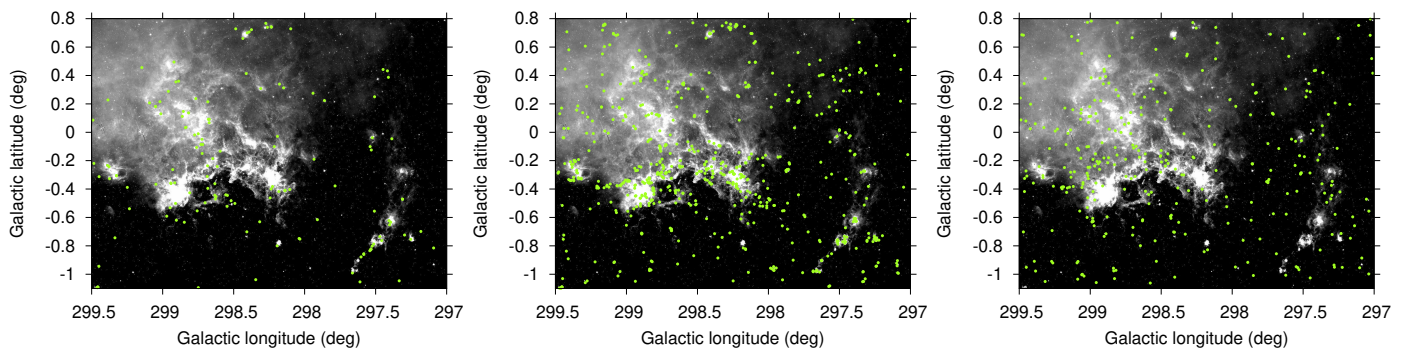


Fig. 7. Spatial distribution of YSO candidates selected according to Koenig & Leisawitz (2014)’s criteria overlaid on the 8 μm band map from Spitzer IRAC. Green dots are sources that fulfil criteria of Class I (left panel), Class II (center panel) or Transition disk (right panel) objects.

Table 3. Calculated correlation dimension (D_c) and corresponding three-dimensional fractal dimension (D_f) for the different classes of YSOs shown in Fig. 7. The number of data points (N) for each sample is also shown.

YSO Class	N	D_c	D_f
All classes	1082	1.74 ± 0.02	$1.9 - 2.0$
Class I	139	1.55 ± 0.07	$1.6 - 1.7$
Class II	627	1.63 ± 0.03	$1.7 - 1.8$
Transition disk	316	1.84 ± 0.04	$2.1 - 2.3$

we use a previously developed and calibrated algorithm that estimates D_c in a precise and accurate manner (Sánchez et al. 2007a; Sánchez & Alfaro 2008). The algorithm constructs the minimum-area convex polygon to delimit the sample and avoid common problems at large scales (whole sample scale). On the other hand, at spatial scales of the order of the mean distance to the nearest neighbour, the distribution looks like a set of isolated points and the obtained D_c values tend to zero (Smith 1988). Our algorithm uses suitable criteria to eliminate poorly estimated data (i.e., bad sampling) and thus to avoid these small-scale issues. Additionally, it applies bootstrapping techniques to estimate an uncertainty associated to D_c . The results from applying this algorithm are presented in Table 3. The estimation of the corresponding three-dimensional fractal dimension D_f is made based on the simulations and results in Sánchez & Alfaro (2008).

The obtained D_f values reveal a certain evolutionary process. Classes I and II exhibit approximately the same value of $D_f \approx 1.7 \pm 0.1$. The slightly smaller value of D_c (and D_f) for the distribution of Class I objects is likely related to the relatively small number of sources ($N = 139$), because it has been shown that below $N \sim 200$ the retrieved value of D_c tends to be smaller than the actual fractal dimension (see Fig. 2 in Sánchez & Alfaro 2008). In contrast, the more evolved Transition Disk objects show a significantly larger dimension with $D_f \approx 2.2 \pm 0.1$. There is evidence for such evolutionary effect, where the initial hierarchical and clumpy structure gradually disappears over time (Elmegreen 2018). In external galaxies, the clumpy structure in the distribution of star formation sites has been observed to change towards smoother distributions as ages increase (Gieles et al. 2008; Sánchez & Alfaro 2008; Bastian et al. 2009; Bonatto & Bica 2010; Sánchez et al. 2010; Menon et al. 2021). At these scales ($\gtrsim 10^3$ pc), the underlying cause may lie in non-turbulent motions acting at a galactic level, on scales on the order of or larger than the scale height of galactic disks (see discussions in Sánchez et al. 2010; Menon et al. 2021). In the case of star clusters, the observed initial substructures also seem to dissipate

with age (Schmeja et al. 2008; Sánchez & Alfaro 2009; Ballone et al. 2020; Daffern-Powell & Parker 2020), but on those spatial scales (~ 10 pc) other physical processes may play important roles and the initial fractal structure is expected to be lost rapidly (Elmegreen 2018), either diluting into more homogeneous distributions in gravitationally unbound clusters or concentrating into radial density distributions in bound clusters. Nevertheless, the associated time scale is not clear and some works suggest that cluster disruption may be a very slow process ($\gtrsim 10$ Myr) in some cases (Hetem & Gregorio-Hetem 2019). In any case, different young clusters may reflect the initial structure of the different clouds from which they formed, and these conditions do not necessarily have to be the same. Therefore, reported correlations between clumpiness and age for large samples of cluster could be contaminated by differences in initial conditions and not correspond to any evolutionary effect. In the case of the Dragonfish complex, we focus on spatial scales of the order of ~ 100 pc, where we detect a significant difference between the distributions of younger and more evolved stars, marking an evolutionary effect. The underlying physical process is still not clear but it may be related to the random stellar motion effect discussed by Elmegreen (2018), in which the initial clumpy structure disappears as stars age due to random turbulent velocity fields acquired at birth.

3.4. Hierarchy of structures

The previous analysis points out that YSOs are distributed in a clumpy manner showing some degree of substructure at different spatial scales. In this section, we address this issue by searching for density substructures in the YSO sample. For this, we apply the algorithm OPTICS (Ordering Points To Identify the Clustering Structure; Ankerst et al. 1999) to perform a global analysis of the density structure of YSOs and retrieve a hierarchy of subclusters. OPTICS extends the clustering algorithm DBSCAN (Ester et al. 1996) to provide a global analysis of the density structure within a region and is especially suited for samples with large density variations. DBSCAN groups points into clusters based on a density associated with two parameters: a minimum number of points N_{min} and a spatial scale ϵ . For each point, the scale ϵ defines a neighbourhood, and N_{min} sets a density requirement for the neighbourhood. DBSCAN identifies clusters as composed of two kinds of points: core points satisfy the density requirement, while border points belong to the ϵ -neighbourhood of a core point but do not satisfy the density requirement themselves. The rest of the points are labelled as noise. In OPTICS, only the N_{min} parameter is fixed and the concept of reachability distance

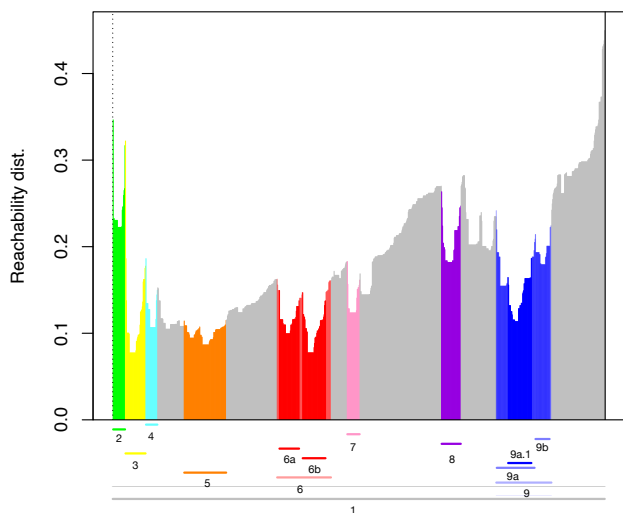


Fig. 8. Reachability plot obtained by OPTICS. The retrieved structures are colour-coded and labelled on the X-axis.

is introduced. We can intuitively interpret the reachability distance between a core point and another point as the minimum distance needed for the second point to be in the ε neighbourhood of the core point, fulfilling the density threshold. OPTICS is not strictly a clustering algorithm, but an analytical tool whose main output is the reachability plot. The reachability plot shows the reachability distance of a reordered sample of points in a diagram where consecutive points are close and the clusters appear as dents or valleys. Based on the reachability plot, we can extract clusters either considering a height ε threshold (obtaining a clustering equivalent to DBSCAN with that ε) or with a slope ξ threshold (where clusters have a specific density ratio to their surroundings). In this work, we use the second approach, as it can detect a hierarchy of structures nested within each other. We set a high value $N_{min} = 20$ to limit the noise in the reachability plot and tested values of $\xi \in [0.01, 0.1]$, finally choosing $\xi = 0.035$ as a good compromise between the detection and the reliability of the clusters retrieved.

Figures 8 and 9 show the reachability plot and a map with the convex hulls of the structures retrieved by OPTICS, in both cases labelled and colour-coded. In Table 4 we display the obtained characteristics of each structure. The whole sample is itself detected as a single structure by OPTICS, tagged and displayed in grey as structure 1 in Fig. 8 but not shown in Fig. 9 and Table 4 for the sake of clarity. The YSO sample exhibits a rich hierarchical structure, as expected from the previous fractal analysis. There are 8 main structures, and amongst them, structures 6 and 9 contain nested substructures. We assign to each structure a level, defined recursively by the number of substructures it contains: structures of level 0 do not contain any other, structures of level 1 contain structures of level 0, structures of level 2 contain structures of level 1, and so on. We find 10 structures of level 0 (namely 2, 3, 4, 5, 6a, 6b, 7, 8, 9a1, and 9b), 2 of level 1 (6 and 9a), 1 of level 2 (9) and 1 of level 3 (structure 1, i.e. the whole sample). By considering a distance of ~ 4 kpc (see Section 3.2.1) and the average equivalent sizes of the structures for each level (shown in Table 4), we obtain that the spatial scales of the structures are of the order of 15, 25, and 25 pc, typical of star-forming regions.

Table 4 also shows the correspondence between our detected structures and star cluster candidates listed in Table 7 of de la Fuente et al. (2016). Out of their 19 candidates, 15 are found

within our structures. Our structure 3 includes the location of the H II region RCW 64 (Caswell & Haynes 1987) that de la Fuente et al. (2016) consider as a foreground region. However, there are 4 objects inside structure 3 with reliable parallaxes from Gaia DR3 which place this structure at a distance of $\sim 3.8 \pm 0.6$ kpc, consistent with our estimation for the whole region (see 3.2.1). Structures 5, 6, and 9 contain three or more known star cluster candidates, and, in the case of the most complex structure 9, its higher level substructure 9a1 contains 5 candidates and displays a clear elongated shape. Even though environmental factors must play some role, the fraction of less evolved Class I sources to the total number of YSOs may yield some hints on the age of the structure (Evans et al. 2009). In fact, the variations in the spatial distribution of objects of different evolutionary stages have been used to investigate the star formation history within specific regions (see e.g. Sung et al. 2009; Venuti et al. 2018; Nony et al. 2021; Flaccomio et al. 2023) For the whole sample, the ratio Class I/YSO is 12.9% which is broadly consistent with the value 14.4% obtained considering only the clustered structures. However, we also identified structures with ratios both larger than 20% and smaller than 5%. Structures 2, 8 and 9a (in particular 9a1) have significantly large Class I/YSO ratios that suggest a higher level of recent star formation, whereas structures 6a and 4 show significantly low ratios, pointing to areas where the star formation activity has declined. These results suggests a complex and varied star formation history in the Dragonfish complex, comprising different events spanning several Myr.

4. Comparison of gas and YSO distributions

A primary goal of this work is to compare the distribution of gas and dust in the Dragonfish region with the distribution of young stars that were born from this gas. Given that we are using the same characterisation tool (the fractal dimension) for gas and for stars, in principle we expect to obtain nearly the same D_f value for both components. The reason is that, at least in the case of ideal monofractal clouds with dimension D_f , the high-density peaks where star formation preferentially takes place are distributed following patterns with the same underlying dimension D_f . On the contrary, our results clearly indicate a scenario in which the distribution of younger objects is much more clumpy ($D_f \approx 1.7$) than the material from which they are forming ($D_f \approx 2.6 - 2.7$).

Evidence supporting or contradicting either of these scenarios is far from being conclusive. There is a lack of works that compare the clustering strength of gas and new-born stars in a direct, quantitative and self-consistent way. At spatial scales smaller than 500 pc, the galaxy M33 is on average more fragmented and irregular than the Milky Way, but its bright young stars are distributed following nearly the same fractal patterns as the molecular gas, both having $D_f \lesssim 1.9$ (Sánchez et al. 2010). In contrast, for the galaxy NGC 7793, Grasha et al. (2018) found that on average star clusters are distributed with a stronger clustering degree than giant molecular clouds over the range 40 – 800 pc; nevertheless, they also found approximately the same degree of clustering when comparing the most massive molecular clouds with the youngest and most massive star clusters. In any case, at spatial scales of the order of the disk scale height, the structure of the interstellar medium generated by turbulent motions may be somehow affected by large-scale galactic dynamics, as discussed in Sánchez et al. (2010) and Menon et al. (2021). Gregorio-Hetem et al. (2015) calculated the clustering in a sample of young star clusters using the Q -parameter (Cartwright & Whitworth 2004) and also estimated

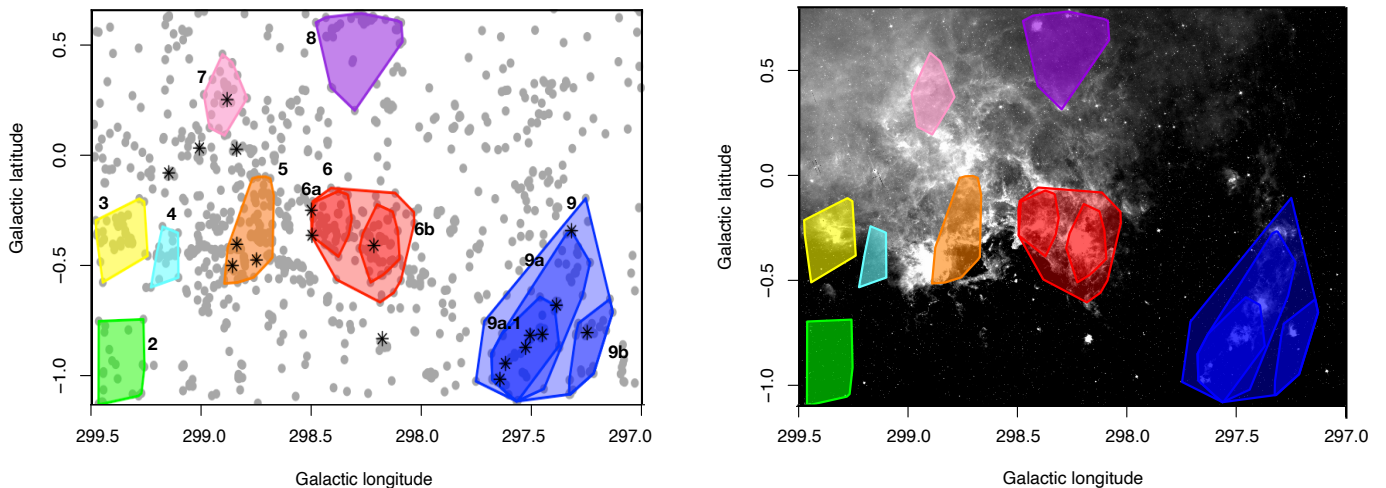


Fig. 9. Left panel: YSOs (grey dots) and convex hulls of the retrieved structures, labelled and coloured as in Fig 8. Black asterisks are candidate or confirmed star clusters taken from Table 7 in de la Fuente et al. (2016). Right panel: Overlap of the convex hulls of structures and the $8 \mu\text{m}$ emission map from Spitzer IRAC.

Table 4. List of the retrieved clustered structures and substructures indicating their IDs, number of sources (N) and the assigned level for each structure, the corresponding mean right ascension and declination in degrees, the equivalent radius in degrees (the radius of a circle having the same area of the associated convex hull), the number of sources for each YSO class, the fraction f_{CI} of Class I sources with respect to the total of YSOs, and cluster candidates in the region listed by de la Fuente et al. (2016).

ID	N	Level	Mean RA	Mean DE	Radius	Class I	Class II	TrDisk	f_{CI}	Candidates
2	27	0	184.90	-63.62	0.24	6	13	8	0.22	
3	45	0	185.02	-62.94	0.21	8	27	10	0.18	
4	26	0	184.54	-63.01	0.13	1	13	12	0.04	
5	93	0	183.71	-62.86	0.23	11	71	11	0.12	Mercer 30, 31 DBSB129
6	119	1	182.67	-62.80	0.36	8	90	21	0.07	
6a	44	0	182.94	-62.77	0.17	0	35	9	0.00	La Serena 24 VVV CI011
6b	51	0	182.46	-62.83	0.18	7	41	3	0.14	DBSB74
7	28	0	184.19	-62.21	0.18	4	14	10	0.14	La Serena 28
8	43	0	182.98	-61.83	0.28	12	25	6	0.28	
9	122	2	180.61	-63.08	0.50	22	74	26	0.18	
9a	84	1	180.74	-63.08	0.36	18	51	15	0.21	La Serena 18 Mercer 28
9a1	52	0	180.85	-63.21	0.25	14	33	5	0.27	La Serena 19, 20, 22 Mercer 29
9b	32	0	180.23	-63.14	0.18	4	20	8	0.12	New Candidate La Serena 17

the perimeter-area-based dimension D_{per} from visual extinction maps in the direction of such clusters. In general, they found that substructures observed for the clusters were very similar to the fractal characteristics of the clouds, although an accurate comparison of the three-dimensional fractal dimension D_f could not be made because projection effects were not properly taken into account. Parker & Dale (2015) performed a direct comparison of the spatial distributions of stars and gas in numerical simulations of molecular clouds using the Q -parameter for both stars and gas. Interestingly, they found that formed stars follow a distribution highly substructured with a value of $Q \sim 0.4 - 0.7$, which corresponds to approximately $D_f \sim 1.8 - 2.3$ (see Fig. 7 in Sánchez & Alfaro 2009), whereas the gas from which stars form had $Q \sim 0.9$, indicating a smooth, concentrated distribution of matter. These results should nevertheless be treated with some caution because, as indicated by Parker & Dale (2015), the Q -parameter may not be an optimal tool for measuring the spatial

distribution of gas, since the pixelated image must be previously converted into a point distribution.

Here, we have found direct and self-consistent evidence that the clustering degree of newly born stars in the Dragonfish region is significantly higher than that of the parent cloud from which stars are forming. We have mentioned that resolution issues (relatively big pixel sizes) could make gas maps look smoother than they actually are, an effect that would not occur for the distribution of stars. However, this is likely not the cause of the observed difference between stars and gas because resolution effects and other factors (signal-to-noise ratio, cloud opacity) have already been calibrated and accounted for to accurately infer D_f from D_{per} (Sánchez et al. 2005, 2007b). If this discrepancy is real, then there could be two possible explanations. On the one hand, the denser gas that is forming stars could be actually clumpier than the distribution of gas throughout the entire region, in concordance with a possible multifractal scenario

that has been proposed for the interstellar medium (Chappell & Scalo 2001). The approach used in this work aims to avoid this issue by focusing on spatial scales of the same order for both the cloud structure and the YSO distribution. On the other hand, the degree of clumpiness may somehow increase during the star formation process. Although some simulations (e.g., Parker & Dale 2015) seem to support this possibility, the physical mechanisms driving this behaviour remain unclear. In simulations of fractal star clusters, Goodwin & Whitworth (2004) demonstrated that an initially homogeneous cluster can develop substructures if it is born with some coherence in the initial velocity field. It is not clear, however, whether such kind of processes could operate at the spatial scale of a whole star-forming complex.

The relationship between the spatial distributions of gas and formed stars remains as an intriguing, and so far unresolved, issue. The problem is non-trivial because the conversion from gas to stars, i.e. the star formation process, involves many physical mechanisms interacting at different spatial scales. Moreover, the formation of stars does not occur synchronously throughout the entire cloud, and the first-formed stars can interact with the surrounding gas modifying its properties and also affecting the distribution of subsequent stars.

5. Conclusions

In this paper, we present a systematic and detailed study of the Dragonfish star-forming region. On the one hand, we used different emission maps to characterise the distribution of gas and dust using fractal analysis. The three-dimensional fractal dimension obtained for the Dragonfish Nebula was $D_f \approx 2.6 - 2.7$, a value that agrees very well with previously reported fractal dimensions for other molecular clouds, namely Orion, Ophiuchus and Perseus. On the other hand, we used photometric information from the AllWISE catalogue to select and study a total of 1082 YSOs in this region. From the parallaxes measured by the Gaia mission for 135 of these sources we derived a distance of $D \sim 4 \pm 1$ kpc to the Dragonfish Complex and from the SED fitting to theoretical models we also determined photospheric temperatures and visual extinctions for 399 sources. Regarding the spatial distribution of YSOs, we identified a clumpy hierarchical assembly of structures and substructures and, moreover, we found that the clumpy structure of younger Class I and Class II sources tends to disappear for the more evolved sources (Transition Disks), suggesting some kind of evolutionary effect. Interestingly, our fractal analysis clearly show that the distribution of younger objects is much more clumpy ($D_f \approx 1.7$) than the distribution of gas from which they formed ($D_f \approx 2.6-2.7$). Although some simulations (e.g., Parker & Dale 2015) seem to support the possibility that newly formed stars exhibit a more clumpy structure than that of their parent cloud, the physical mechanisms behind this behaviour remain unclear. In order to clarify this issue, it would be helpful to use strategies such as the one proposed in this work, in which suitable and well-calibrated tools are used to simultaneously quantify the structure of both gas and stars in a relatively large sample of star-forming complexes.

Acknowledgements. We want to thank the referee for his/her helpful comments, which improved this paper. We acknowledge financial support from Universidad Internacional de Valencia (VIU) through project VIU24003. The work of EN was supported by project VIU24007, funded by the research center ESENCIA of VIU. JBC was supported by projects PID2020-117404GB-C22, funded by MCIN/AEI, CIPROM/2022/64, funded by the Generalitat Valenciana, and by the Astrophysics and High Energy Physics programme by MCIN, with funding from European Union NextGenerationEU (PRTR-C17.I1) and the Generalitat Valenciana through grant ASFAE/2022/018. This research made use of Montage, that it is funded by the National Science Foundation under Grant Num-

ber ACI-1440620, and was previously funded by the National Aeronautics and Space Administration's Earth Science Technology Office, Computation Technologies Project, under Cooperative Agreement Number NCC5-626 between NASA and the California Institute of Technology. We have made extensive use of VOSA, developed under the Spanish Virtual Observatory project funded by MCIN/AEI/10.13039/501100011033/ through grant PID2020-112949GB-I00. We also have used the tool TOPCAT (Taylor 2005) and the NASA's Astrophysics Data System.

References

- Allison, R. J., Goodwin, S. P., Parker, R. J., Portegies Zwart, S. F., & de Grijs, R. 2010, *MNRAS*, 407, 1098
- Ankerst, M., Breunig, M. M., Kriegel, H.-P., & Sander, J. 1999, *SIGMOD Rec.*, 28, 49
- Arnold, B., Wright, N. J., & Parker, R. J. 2022, *MNRAS*, 515, 2266
- Ballone, A., Mapelli, M., Di Carlo, U. N., et al. 2020, *MNRAS*, 496, 49
- Bally, J. 2016, *ARA&A*, 54, 491
- Bastian, N., Gieles, M., Ercolano, B., & Gutermuth, R. 2009, *MNRAS*, 392, 868
- Bates, M. L. & Whitworth, A. P. 2023, *MNRAS*, 523, 233
- Bates, M. L., Whitworth, A. P., & Lomax, O. D. 2020, *MNRAS*, 493, 161
- Bayo, A., Rodrigo, C., Barrado Y Navascués, D., et al. 2008, *A&A*, 492, 277
- Bazell, D. & Desert, F. X. 1988, *ApJ*, 333, 353
- Beattie, J. R., Federrath, C., & Klessen, R. S. 2019, *MNRAS*, 487, 2070
- Bergin, E. A. & Tafalla, M. 2007, *ARA&A*, 45, 339
- Blaylock-Squibbs, G. A., Parker, R. J., Buckner, A. S. M., & Güdel, M. 2022, *MNRAS*, 510, 2864
- Bonatto, C. & Bica, E. 2010, *MNRAS*, 403, 996
- Buckner, A. S. M., Khorrami, Z., Khalaj, P., et al. 2019, *A&A*, 622, A184
- Caffau, E., Ludwig, H. G., Steffen, M., Freytag, B., & Bonifacio, P. 2011, *Sol. Phys.*, 268, 255
- Cartwright, A. & Whitworth, A. P. 2004, *MNRAS*, 348, 589
- Castelli, F., Gratton, R. G., & Kurucz, R. L. 1997, *A&A*, 318, 841
- Caswell, J. L. & Haynes, R. F. 1987, *A&A*, 171, 261
- Chappell, D. & Scalo, J. 2001, *ApJ*, 551, 712
- Clarke, S. D., Jaffa, S. E., & Whitworth, A. P. 2022, *MNRAS*, 516, 2782
- Colombo, D., Rosolowsky, E., Ginsburg, A., Duarte-Cabral, A., & Hughes, A. 2015, *MNRAS*, 454, 2067
- Cutri, R. M., Wright, E. L., Conrow, T., et al. 2021, *VizieR Online Data Catalog: AllWISE Data Release (Cutri+ 2013)*, *VizieR On-line Data Catalog: II/328*. Originally published in: *IPAC/Caltech (2013)*
- Daffern-Powell, E. C. & Parker, R. J. 2020, *MNRAS*, 493, 4925
- De Buizer, J. M., Lim, W., Karnath, N., Radomski, J. T., & Bonne, L. 2022, *ApJ*, 933, 60
- de la Fuente, D., Najarro, F., Borissova, J., et al. 2016, *A&A*, 589, A69
- de La Fuente Marcos, R. & de La Fuente Marcos, C. 2006, *A&A*, 452, 163
- Dib, S., Bontemps, S., Schneider, N., et al. 2020, *A&A*, 642, A177
- Dickman, R. L., Horvath, M. A., & Margulis, M. 1990, *ApJ*, 365, 586
- Draine, B. T. & Li, A. 2007, *ApJ*, 657, 810
- Elia, D., Strafella, F., Dib, S., et al. 2018, *MNRAS*, 481, 509
- Elia, D., Strafella, F., Schneider, N., et al. 2014, *ApJ*, 788, 3
- Elmegreen, B. G. 2018, *ApJ*, 853, 88
- Elmegreen, B. G. & Elmegreen, D. M. 2001, *AJ*, 121, 1507
- Elmegreen, B. G. & Scalo, J. 2004, *ARA&A*, 42, 211
- Ester, M., Kriegel, H.-P., Sander, J., & Xu, X. 1996, in *Proceedings of the Second International Conference on Knowledge Discovery and Data Mining, KDD'96 (AAAI Press)*, 226–231
- Evans, Neal J., I., Dunham, M. M., Jørgensen, J. K., et al. 2009, *ApJS*, 181, 321
- Falgarone, E., Phillips, T. G., & Walker, C. K. 1991, *ApJ*, 378, 186
- Flaccomio, E., Micela, G., Peres, G., et al. 2023, *A&A*, 670, A37
- Ghazzali, N., Joncas, G., & Jean, S. 1999, *ApJ*, 511, 242
- Gieles, M., Bastian, N., & Ercolano, B. 2008, *MNRAS*, 391, L93
- Gomez, M., Hartmann, L., Kenyon, S. J., & Hewett, R. 1993, *AJ*, 105, 1927
- González, M., Joncour, I., Buckner, A. S. M., et al. 2021, *A&A*, 647, A14
- Goodwin, S. P. & Whitworth, A. P. 2004, *A&A*, 413, 929
- Grasha, K., Calzetti, D., Bittle, L., et al. 2018, *MNRAS*, 481, 1016
- Grassberger, P. & Procaccia, I. 1983, *Phys. Rev. Lett.*, 50, 346
- Gregorio-Hetem, J., Hetem, A., Santos-Silva, T., & Fernandes, B. 2015, *MNRAS*, 448, 2504
- Hartmann, L. 2002, *ApJ*, 578, 914
- Hetem, A. & Gregorio-Hetem, J. 2019, *MNRAS*, 490, 2521
- Hetem, A., J. & Lepine, J. R. D. 1993, *A&A*, 270, 451
- Houllahan, P. & Scalo, J. 1992, *ApJ*, 393, 172
- Jaffa, S. E., Dale, J., Krause, M., & Clarke, S. D. 2022, *MNRAS*, 511, 2702
- Jaffa, S. E., Whitworth, A. P., Clarke, S. D., & Howard, A. D. P. 2018, *MNRAS*, 477, 1940
- Jaffa, S. E., Whitworth, A. P., & Lomax, O. 2017, *MNRAS*, 466, 1082
- Khalil, A., Joncas, G., & Nekka, F. 2004, *ApJ*, 601, 352

- Khalil, A., Joncas, G., Nekka, F., Kestener, P., & Arneodo, A. 2006, *ApJS*, 165, 512
- Koenig, X. P. & Leisawitz, D. T. 2014, *ApJ*, 791, 131
- Kraus, A. L. & Hillenbrand, L. A. 2008, *ApJ*, 686, L111
- Kuhn, M. A., de Souza, R. S., Krone-Martins, A., et al. 2021, *ApJS*, 254, 33
- Larson, R. B. 1981, *MNRAS*, 194, 809
- Larson, R. B. 1995, *MNRAS*, 272, 213
- Lee, Y., Li, D., Kim, Y. S., et al. 2016, *Journal of Korean Astronomical Society*, 49, 255
- Lindgren, L., Bastian, U., Biermann, M., et al. 2021, *A&A*, 649, A4
- Lumsden, S. L., Hoare, M. G., Urquhart, J. S., et al. 2013, *ApJS*, 208, 11
- Mandelbrot, B. B. 1983, *The fractal geometry of nature* (Freeman, New York)
- Marchuk, A. A., Smirnov, A. A., Mosenkov, A. V., et al. 2021, *MNRAS*, 508, 5825
- Marton, G., Tóth, L. V., Paladini, R., et al. 2016, *MNRAS*, 458, 3479
- McKee, C. F. & Ostriker, E. C. 2007, *ARA&A*, 45, 565
- Menon, S. H., Grasha, K., Elmegreen, B. G., et al. 2021, *MNRAS*, 507, 5542
- Moisés, A. P., Damineli, A., Figuerêdo, E., et al. 2011, *MNRAS*, 411, 705
- Nony, T., Robitaille, J. F., Motte, F., et al. 2021, *A&A*, 645, A94
- Ochsenbein, F., Bauer, P., & Marcout, J. 2000, *A&AS*, 143, 23
- Parker, R. J. & Dale, J. E. 2015, *MNRAS*, 451, 3664
- Planck Collaboration, Adam, R., Ade, P. A. R., et al. 2016, *A&A*, 594, A10
- Planck Collaboration, Ade, P. A. R., Aghanim, N., et al. 2011, *A&A*, 536, A1
- Rahman, M., Matzner, C., & Moon, D.-S. 2011a, *ApJ*, 728, L37
- Rahman, M., Moon, D.-S., & Matzner, C. D. 2011b, *ApJ*, 743, L28
- Rate, G., Crowther, P. A., & Parker, R. J. 2020, *MNRAS*, 495, 1209
- Rimoldini, L., Holl, B., Gavras, P., et al. 2023, *A&A*, 674, A14
- Robitaille, J. F., Joncas, G., & Khalil, A. 2010, *MNRAS*, 405, 638
- Rosolowsky, E. W., Pineda, J. E., Kauffmann, J., & Goodman, A. A. 2008, *ApJ*, 679, 1338
- Russeil, D. 1997, *A&A*, 319, 788
- Sánchez, N., Añez, N., Alfaro, E. J., & Crone Odekon, M. 2010, *ApJ*, 720, 541
- Sánchez, N. & Alfaro, E. J. 2008, *ApJS*, 178, 1
- Sánchez, N. & Alfaro, E. J. 2009, *ApJ*, 696, 2086
- Sánchez, N., Alfaro, E. J., Elias, F., Delgado, A. J., & Cabrera-Caño, J. 2007a, *ApJ*, 667, 213
- Sánchez, N., Alfaro, E. J., & Pérez, E. 2005, *ApJ*, 625, 849
- Sánchez, N., Alfaro, E. J., & Pérez, E. 2007b, *ApJ*, 656, 222
- Sánchez, N. M. & Parravano, A. 1999, *ApJ*, 510, 795
- Schinnerer, E., Meidt, S. E., Pety, J., et al. 2013, *ApJ*, 779, 42
- Schmeja, S., Kumar, M. S. N., & Ferreira, B. 2008, *MNRAS*, 389, 1209
- Silverman, B. W. 1986, *Density estimation for statistics and data analysis* (Chapman and Hall/CRC, London)
- Simon, M. 1997, *ApJ*, 482, L81
- Smith, J. D., Dale, J. E., Jaffa, S. E., & Krause, M. G. H. 2022, *MNRAS*, 516, 4212
- Smith, L. A. 1988, *Physics Letters A*, 133, 283
- Stutzki, J., Bensch, F., Heithausen, A., Ossenkopf, V., & Zielinsky, M. 1998, *A&A*, 336, 697
- Sun, J., Gutermuth, R. A., Wang, H., Zhang, S., & Long, M. 2022, *MNRAS*, 516, 5258
- Sung, H., Stauffer, J. R., & Bessell, M. S. 2009, *AJ*, 138, 1116
- Taylor, M. B. 2005, in *Astronomical Society of the Pacific Conference Series*, Vol. 347, *Astronomical Data Analysis Software and Systems XIV*, ed. P. Shopbell, M. Britton, & R. Ebert, 29
- Venuti, L., Prisinzano, L., Sacco, G. G., et al. 2018, *A&A*, 609, A10
- Vogelaar, M. G. R. & Wakker, B. P. 1994, *A&A*, 291, 557
- Werner, M. W., Roellig, T. L., Low, F. J., et al. 2004, *ApJS*, 154, 1
- Wright, E. L., Eisenhardt, P. R. M., Mainzer, A. K., et al. 2010, *AJ*, 140, 1868
- Zhang, C., Zhang, G.-Y., Li, J.-Z., & Yuan, J.-H. 2023, *ApJS*, 264, 24